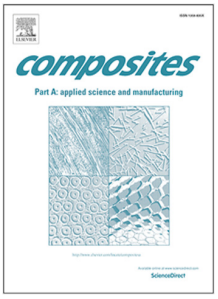
Journal Pre-proof



Thermal history and multi-scale analyses of 3D-printed continuous carbon fibre composites

Fei Liu, Shenru Wang, Jie Zhang, Wuxiang Zhang, Laurens Snels, David Seveno, Eleonora Ferraris, Jan Ivens

PII: S1359-835X(25)00352-5
DOI: https://doi.org/10.1016/j.compositesa.2025.109058
Reference: JCOMA 109058

To appear in: *Composites Part A*

Received date : 3 September 2024
Revised date : 17 May 2025
Accepted date : 22 May 2025

Please cite this article as: F. Liu, S. Wang, J. Zhang et al., Thermal history and multi-scale analyses of 3D-printed continuous carbon fibre composites. *Composites Part A* (2025), doi: https://doi.org/10.1016/j.compositesa.2025.109058.

This is a PDF file of an article that has undergone enhancements after acceptance, such as the addition of a cover page and metadata, and formatting for readability, but it is not yet the definitive version of record. This version will undergo additional copyediting, typesetting and review before it is published in its final form, but we are providing this version to give early visibility of the article. Please note that, during the production process, errors may be discovered which could affect the content, and all legal disclaimers that apply to the journal pertain.

© 2025 Published by Elsevier Ltd.

Journal Pre-proof

Thermal history and multi-scale analyses of 3D-printed continuous carbon fibre composites

Fei Liu[a,*], Shenru Wang[a,*], Jie Zhang[b,c], Wuxiang Zhang[a,**], Laurens Snels[d], David Seveno[d], Eleonora Ferraris[b], Jan Ivens[e,**]

[a]School of Mechanical Engineering and Automation, Beihang University, Beijing 100191, China
[b]Department of Mechanical Engineering, KU Leuven Campus De Nayer, Sint-Katelijne-Waver 2860, Belgium
[c]Members Flanders Make, Leuven 3000, Belgium
[d]Department of Materials Engineering, KU Leuven, Leuven 3000, Belgium
[e]Department of Materials Engineering, KU Leuven Campus De Nayer, Sint-Katelijne-Waver 2860, Belgium

Abstract

The interfacial bonding properties of 3D-printed continuous carbon fibre composites are strongly influenced by the thermal history related to various printing parameters. However, there remains a gap in understanding the effects of thermal history on specific properties across multiple scales. This study addresses the gap in understanding these effects across multiple scales by developing a numerical temperature model, a computational fluid dynamics model and a representative volume element approach for the deposition process. The temperature model was validated against experimental profiles, where the maximum mean absolute difference is 4.5 °C, and the flexural performance with 29.8% error is obtained. Through two models, we found that print speed and layer thickness have a significant impact on interfacial bonding and defect formation. This study provides insights into the relationship between thermal history and interfacial behaviour, aiding machine developers in enhancing structural performance, and promoting the application of high-quality composites.

Keywords: carbon fibres, 3D printing, thermal history, computational fluid dynamics

1. Introduction

3D printing technology encompasses various manufacturing methods used to produce components, ranging from prototypes to fully functional parts with complex geometries [1, 2]. Among them, material extrusion (MEX) printing, especially fused filament fabrication (FFF) is the predominant technology for producing continuous carbon fibre-reinforced composites (CFRCs) structures due to its high design freedom, shortened product development cycle, relatively low costs, material diversity and ease of use [3]. Thanks to the carbon fibre it offers excellent mechanical properties by integrating multiple materials throughout the manufacturing process, and is renowned in a wide industrial applications such as healthcare [4, 5], construction [6] and transportation [7]. The FFF printing process is temperature-driven, facilitating the liquefaction of the extruded material for smooth flow through the nozzle and subsequent bonding with a preceding layer [8]. Specifically, the construction of a structure is limited within a small area around the printing nozzle, where multiple materials are simultaneously heated to molten states and rapidly cooled less than a second to bond with the previous layer before solidification [9].

Due to the localised and transient heating introduced by the extrusion nozzle, along with rapid cooling and re-heating cycles following the print trajectory, the manufacturing process occurs under highly non-isothermal conditions. The rapid phase transitions, steep thermal gradients, and surface tension effects govern the behaviour of deposited material and ultimately determine the final geometry and quality characteristics of the monolithic structure. Unforeseen defects, weak bonding, and misalignment of the FFF-printed parts within the inter-/intra- layers are closely related to and process parameters [10–12]. Consequently, particular emphasis is placed on controlling and optimising the process parameters [12–16]. Several studies have analysed the influence of various process parameters, such as temperature, speed, layer thickness, print orientation, compaction force and curing temperature, etc, on the tensile [17, 18], compressive [19] and flexural [20] behaviour of printed parts. Other studies have focused on the microstructure [21], interface forming [22] and failure modes [10, 23] of printed CFRCs. In these publications, it was proved that the mechanical behaviour of the printed parts is highly constrained by process-induced defects.

As research has progressed, increasing attention has been devoted to understanding the underlying process mechanisms, specifically, how process parameters affect material behaviour during printing, and how these interactions ultimately influence the quality of printed components. A deeper understanding of these mechanisms reduces the demand for extensive experimental testing when exploring new materials or structural designs, thereby accelerating the identification of optimal process parameters. To investigate the dynamic nature of the printing pro-

*Fei Liu and Shenru Wang are co-first authors.
**Correspondence: Jan Ivens (jan.ivens@kuleuven.be), KU Leuven, Campus De Nayer, Sint-Katelijne-Waver 2860, Belgium. Wuxiang Zhang (zhangwuxiang@buaa.edu.cn), Beihang University, Beijing 100191, China.

cess, a variety of advanced *in-situ* monitoring techniques have been employed. Caltanissetta et al. [24] proposed a data-driven method for *in-situ* monitoring of thermal profiles, enabling automatic detection of local temperature inhomogeneities during printing, allowing for targeted process optimisation. Holzmond et al. [25] utilised three-dimensional digital image correlation to achieve *in-situ* monitoring of warpage deformation in printed structures. Badarinath et al. [26] combined infrared thermography with a vision-based approach to simultaneously monitor nozzle temperature and the width of extruded resin, using their correlation to improve printing quality. Li et al. [27] and Moretti et al.[28] applied machine learning and digital twin technologies to monitor the geometry of parts during printing, thereby enhancing dimensional accuracy. Yang et al. [29] employed X-ray micro-tomography to scan the in-nozzle melted filament and extruded printing bead during the printing process, enabling them to track the evolution of fibres and pores throughout printing. These *in-situ* monitoring efforts have provided valuable data for studying process mechanisms. However, such experimental setups significantly increase system complexity and remain limited in their ability to capture microscale material behaviours such as flow dynamics and phase transitions. Besides, they often struggle to maintain measurement accuracy and consistency due to the continually changing geometry during the printing process.

To better understand the relationship between process parameters and resin flow, theoretical modelling and simulation offer an attractive approach to provide further insight. Zhang et al. [30] developed a three-dimensional thermal model of the printing process using the finite difference method and investigated the impregnation mechanism of continuous fibre under different printing conditions by incorporating Darcy's law. Phan et al. [31] applied computational fluid dynamics (CFD) to simulate the flow behaviour of molten resin inside the nozzle, aiming to understand the material melting and pressurization mechanisms. Miri et al. [32] employed the Ericksen anisotropic flow model to describe the deformation and flow of CFRCs during printing, and determined the optimal spacing between printed strands based on simulation results. Fu et al.[33] used CFD to study the relationship between printing temperature, stacking strategy, and porosity formation in printed parts. Yang et al. [34] developed a fluid–structure interaction model of CFRCs flow within the nozzle using the smoothed particle hydrodynamics and the discrete element method, which guided the nozzle design improvements. Comminal et al. [35] presented a CFD model to quantify the effect of the void and the print speed on the geometry of a single deposited strand. Xia et al. [36] established a numerical model for resin extrusion and deposition, and discussed the influence of resin viscoelasticity on the size and shape of extruded beads. Ghnatios et al. [37] established a numerical model via proper generalized decomposition to predict the wrapping deformation at the edges and demonstrated the impact of bed temperature, nozzle temperature and print speed on the maximum deformation. With [34], a coupled particle method was proposed to capture the movement and deformation of carbon fibre during the squeezing process. Their study only analysed the interaction among the print head, nozzle, and print bed, which shed light on the beginning of the printing process. Based on that, Wang et al. [38] developed a theoretical impregnation model and analysed the impregnation behaviour during the FFF printing process. It is worth emphasising that the positive correlation between impregnation percentage and mechanical performance, is influenced by print speed, temperature, and layer thickness. As reported, these studies have focused on establishing mathematical correlations between process parameters and the mechanical properties of FFF-fabricated CFRCs and provided valuable insights that can enhance the additive manufacturing of components with optimised mechanical properties; however, simulations targeting the printing of complete structural parts remain scarce. Additionally, a direct linkage between process parameters and performance without clarifying the thermal history and interfacial behaviour [39, 40] can fall short of providing a comprehensive understanding of their coupled effects from the standpoint of the manufacturing process.

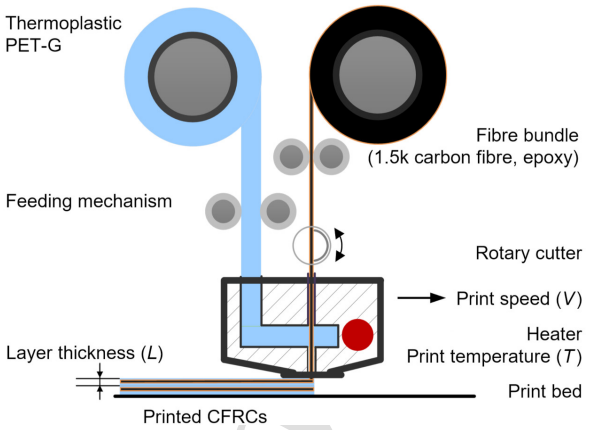


Figure 1: The schematic of Anisoprint printing process for continuous carbon fibre-reinforced composites (CFRCs).

The motivation of this study is thus to establish a connection among process parameters, thermal history, and the mechanical properties of the continuous carbon fibre-reinforced composite materials. Firstly, a numerical thermal transfer model is built for anisotropic materials, and assessed through a temperature monitoring approach. A CFD model is then presented to reproduce the flow behaviour of molten resin during the printing process. Moreover, the calculated void content from CFD model is used to predict the effective material properties of the printed composites mechanical properties through a relative representative element (RVE) model. These properties, accounting for void-induced effects, are then used as input for a three-point bending finite element model to capture the influence of processing conditions on mechanical performance. Literately, the influence of two process parameters on interfacial behaviour and defect distribution along the inter/intra layers in multi-scale are analysed. This study provides a theoretical foundation and approaches for establishing the future digital twin system, implementing of real-time control and optimising strategies for printing processes.

Journal Pre-proof

2. Material and methods

2.1. Printing materials and equipment

In this study, an Anisoprint Composer A3 was utilised to fabricate the continuous carbon fibre (CCF) reinforced thermoset and thermoplastic composites. The feedstock material was a 1.5k CCF bundle pre-impregnated with thermoset epoxy resin, wherein the fibre volume ratio in the fibre bundle is 60% and the epoxy is fully cured before printing process [11]. The material properties of carbon fibre bundles are shown in Table 2. Furthermore, a thermoplastic polyethylene terephthalate glycol (PET-G, REC3d, Russia) was chosen to coat the fibre bundle composite filament in the printing process. The epoxy of carbon fibre bundles in our study is based on an epoxy matrix that is fully cured prior to printing [11]. Fig. 1 illustrates the printing sketch map presenting the printing parameters set to fabricate the specimen. During the printing, a good wetting and mechanical interlocking at the interface between PETG and epoxy, with no significant signs of delamination or voids, is assumed.

2.2. Surface tension and viscosity tests

2.2.1. Surface tension test

The flow of PET-G in air involves the dynamic behaviour of the gas-liquid interface, where surface tension plays a critical role. In CFD simulations, surface tension is incorporated as a source term in the momentum conservation, directly influencing the resin flow behaviour. Therefore, this study conducted experiments to measure the surface tension of PET-G at different printing temperatures. An OCA50 (DataPhysics, Germany) equipped with a high-temperature dosing unit NHD700 and chamber TEC700 was used to measure the surface tension of PET-G at a controlled temperature in nitrogen atmosphere (flow rate 40 mL/min) to prevent polymer degradation. The PET-G filament was loaded into a ceramic cannula with a 2 mm nozzle. Afterwards, the cannula and chamber were heated to 210, 220, 230, 240, and 250 °C, respectively. The calculation of the surface tension required the polymer's density and outer nozzle diameter as inputs. The calculation was performed with the SCA20 software (Dataphysics, Germany), using Laplace-Young fitting of the axisymmetric droplet to determine its shape. Three droplets were measured at each temperature [41].

2.2.2. Viscosity test

Since carbon fibre is fully impregnated with thermoset epoxy before the printing, only the viscosity of PETG is affected by the varying temperature and shear rate during the printing process [42]. To characterise the temperature and shear-rate-dependent viscosity behaviour of PET-G, rheology testing was performed according to ASTM D7605-11(2022) [43] at multiple temperatures (210, 220, 230, 240, 250 °C) and shear rates (0.01–500 s^{-1}) using the Discovery HR 20 rheometer (TA Instruments, USA). These experimentally measured results were essential to the calculation and verification of the numerical model.

2.3. Temperature monitoring

Online temperature monitoring of the material deposition process was conducted with an Optris PI640 infrared (IR) camera (Optris GmbH, Germany). The IR camera records the infrared radiation emitted by an object and converts it into a visible image or video. The technical data of the IR camera are given in Table 1. Various factors, such as the surface reflectivity of the collected material and the view angle influence the accuracy of temperature data captured by IR cameras. Therefore, the camera was mounted on the print bed with a flexible clamper (Fig. 2). For a printed object aligned with the Cartesian coordinate system of the machine, the camera subsequently captures the variations in temperature within the frontal *xoz* plane of the object, ensuring accurate monitoring of temperature fluctuations for subsequent data analysis and processing.

Table 1: Technical data of infrared (IR) camera.

Parameter	Technical data
Wavelength range	7.5–13 µm
Sampling frequency	32 Hz
Optical resolution	640×480 pixels
Spatial resolution	31.25 µm/pixel
Field of view	20×15 mm^2
Working distance	85 mm
Accuracy	±2 °C or ±2%, whichever is greater

To minimize the reflection of the thermal signal of the object, the nozzle was effectively shielded, and the build platform was covered with a tape coated with a specialized "non-reflective" paint (reflectivity < 0.08, LabIR® Paint, HERP-LT-MWIR-BK-11), which effectively reducing any potential interference caused by reflected heat signatures. The emissivity value of infrared camera was also calibrated using a thermocouple before the online temperature monitoring. To calibrate the infrared camera, the temperature of the printing bed is set to 60 °C, and one end of the thermocouple is arranged on the surface of the printed sample waiting for the temperature to stabilise. By adjusting the emissivity value to ensure that the temperature of the infrared camera is consistent with the thermocouple, camera calibration was achieved. In this case, the material emissivity $\varepsilon = 0.82$ was fixed.

3. Numerical simulation methodology

To provide valuable insights into the effect of process parameters on the thermal and fluid dynamics during 3D printing, as well as the mechanical properties of the printed parts, we conducted a numerical simulation strategy focusing on the heat transfer and flow behaviour during the printing process. The comparison between experimental observations and simulation results highlights the accuracy of the numerical predictions and enhances our understanding of the printing process. A heat transfer model based on the finite difference method [44] was performed to analyse the relationship between the process parameters and the thermal history evolution during the manufacturing of the CFRP part. The model solved the initial and

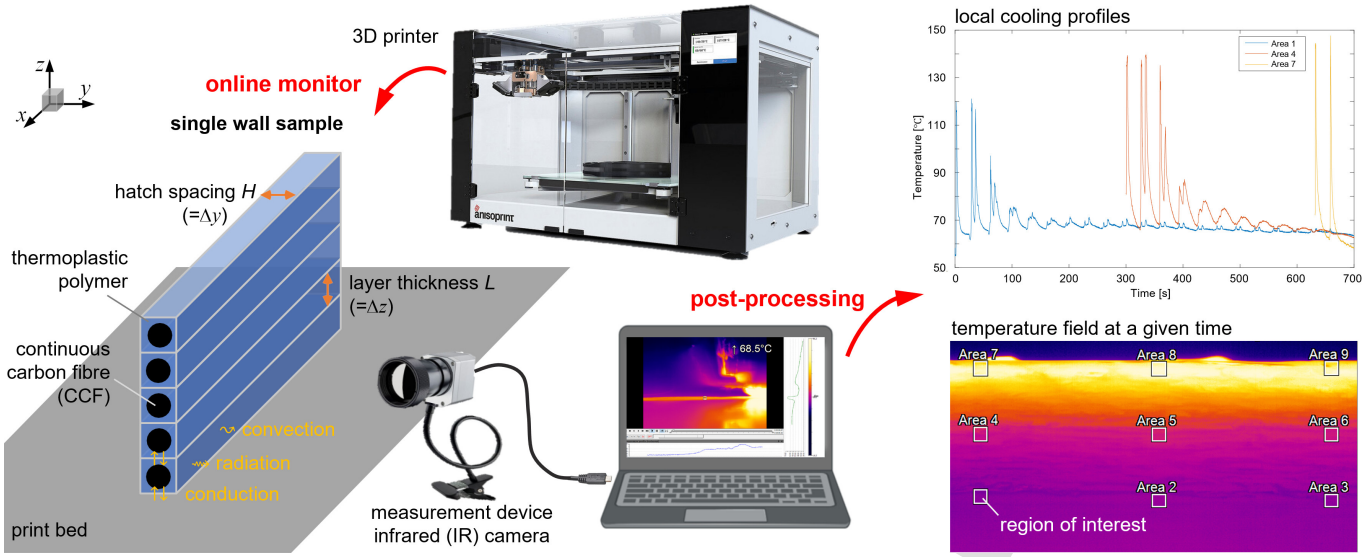


Figure 2: Overview of the research elements: diagram of the experimental sample, picture of the 3D printer and representative image of and the results of the thermal monitoring with an Optris PI640 infrared (IR) camera. Drawing not to scale, for illustration purposes only.

boundary value problem of anisotropic heat conduction in an evolving geometry, subjected to location-wise initial condition (temperature of extrudates agreeing with the nominal nozzle temperature) and combined thermal boundary conditions (convection with the nearby air and radiation heat transfer with the far environment for all free surfaces; Dirichlet boundary for the bottom surface of the first layer contacting the build plate).

Additionally, the CFD method was employed to investigate the impact of process parameters on the printing morphology, with a particular focus on the interfilamentous void morphology. Utilizing the void content obtained from the CFD model, an RVE model considering the proportion of fibre, resin, and void was built to predict the effective material properties of the printed parts. Finally, the predicted material properties were imported into a three-point blending simulation for modelling verification because three-point bending tests is more sensitive to defects of the printed part rather than tensile testing.

3.1. Numerical thermal transfer modelling

Numerical thermal transfer modelling involves the development and application of mathematical models to simulate heat transfer processes during FFF printing. The thermal transfer model is crucial in predicting and understanding the thermal behaviours in various systems enabling engineers and scientists to improve efficiency, especially supporting engineers in precisely defining hardware control parameters, ensuring consistent and reliable composite consolidation. Firstly, the governing partial differential equation (PDE) for heat transfers in the printed part is presented [44]:

$$\rho c_{\mathrm{p}} \frac{\partial T^*(\mathbf{r},t)}{\partial t} = k_x \frac{\partial^2 T^*}{\partial x^2} + k_y \frac{\partial^2 T^*}{\partial y^2} + k_z \frac{\partial^2 T^*}{\partial z^2}, \ \mathbf{r} = (x,y,z) \in \Omega(t) \tag{1}$$

where, the temperature $T^*(\mathbf{r},t)$ depends on both the spatial location $\mathbf{r} = (x,y,z)$ and time t. The 3D geometry of the part $\Omega = \Omega(t)$ evolves with time, which reflects the additive nature of the manufacturing process. The conductivity of the composite strand shows anisotropy due to the existence of the continuous fibre, i.e., $k_x > k_y$ and $k_x > k_z$. The density ρ and heat capacity c_{p} were calculated from those of the CCF phase and PET-G phase, as shown in Table 2. Notably, the CCF exhibits a strong conduction anisotropy in the direction along and perpendicular to the fibre orientation. Such conduction anisotropy is inherent in the strand composite. We assume the properties of the deposited strand obey the rule of mixture

$$X = \sum_i V_{fi} \cdot x_i, \tag{2}$$

where the resultant property X is a volume content V_{fi} weighted average of the property x_i each component. Therefore, the longitudinal thermal conductivity is 2.0579 W/mK, the transverse thermal conductivity is 0.5378 W/mK, heat capacity is 1.122 J/gK, and the density is 1.53 g/cm^3.

The initial condition is described for each strand section upon deposition, such that the strand has a uniform temperature agreeing with the nominal nozzle temperature. The boundary condition is described for all free surfaces. The resultant outward flux density combines thermal convection with the nearby air and thermal radiation with the far environment. The convection coefficient took the average value of 40 W/m^{2}K which is commonly used [45].

The corresponding analysis and experiments were conducted on a single-wall (1-track) with 5 layers, to thoroughly analyse the impact of various process parameters on the thermal history. First, the thermal transfer model was verified by experiments under nozzle temperature variation. Then, we focused on the process parameters: print speed (V), and layer thickness (L). The investigation adhered to a one-factor variation method, where each parameter was systematically varied across multiple

Journal Pre-proof

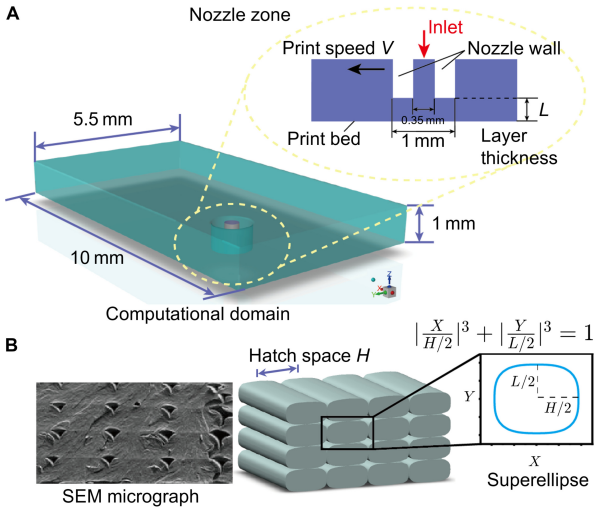


Figure 3: (**A**) CFD schematic diagram of the printing process; (**B**) Superellipse assumption of the cross-section in the printed part [46].

Table 2: Material properties of PET-G, continuous carbon fibre (CCF), and air [47–50].

Component	Property	Value
PET-G	Density ρ_1	1.3 g/cm^3
	Heat capacity c_{p1}	1.25 J/gK
	Thermal conductivity k_1	0.2 W/mK
CCF	Density ρ_2	1.71 g/cm^3
	Heat capacity c_{p2}	1.023 J/gK
	Longitudinal conductivity $k_{2,\parallel}$	3.5 W/mK
	Transverse conductivity $k_{2,\perp}$	0.8 W/mK
	E_1	154 GPa
	E_2	7.5 GPa
	G_{12}	4.5 GPa
	ν	0.31
Air	Density ρ_a	1.225 kg/m^3
	Heat capacity $c_{p,a}$	1.00643 J/gK
	Thermal conductivity k_a	0.0242 W/mK

levels while keeping all other process settings constant. In the following cases, the hatch spacing is maintained at 0.75 mm, with a print bed temperature of 60 °C, and a printed length of 100 mm for each layer. This approach allowed us to isolate the effects of each parameter on the thermal history and microstructure, as summarised in Table 3.

During the simulations, the numerical scheme showed a convergence problem due to the effective thermal conductivity being too high to meet the stability criteria [51], hence the temperature similarity rule was applied progressively with a scaling factor of 2 whenever the stability issue happens (meaning the length and travelling speed were doubled). An optimised mesh size was used in the simulations. The boundary contacting the build plate took the Dirichlet boundary condition. The temperature model was solved in the open-access software T4F3 (version 1.03) [44] based on a sequential union of cuboid voxels according to the selective deposition.

Table 3: 3D printing process parameters used in the thermal modelling.

Target parameter	Value	Constant parameter
Nozzle temperature T [°C]	210, 230, 250	V 300, L 0.4, H 0.75
Print speed V [mm/min]	150, 300, 600	T 230, L 0.4, H 0.75
Layer thickness L [mm]	0.4, 0.7, 0.9	T 230, V 300, H 0.75

3.2. *Computational fluid dynamics*

3.2.1. *CFD model description*

The flow behaviour and printing morphology of the printing process are simulated using a CFD model in Ansys® Fluent, v2023 [49]. It is observed that since the fibres are already pre-impregnated, the PET-G primarily melts within the nozzle and then coats the fibre surfaces. Consequently, the flow characteristics of the PET-G resin are one of the main factors influencing the internal features of the structural components. Therefore, to simplify the CFD model, we primarily simulate the resin flow and solidification processes, analysing the morphology and void characteristics between different strands within and between layers. The schematic diagram and feature size of the numerical model are shown in Fig. 3**A**, and its initial computational domain size is $10\times5.5\times1$ mm^3. The gap distance between the nozzle and the print bed is the layer thickness of L. This model adopts the transient solution and uses the hexahedral mesh with a size of 0.05 mm. In this model, the molten resin is extruded from the inlet at a linear feed speed of V_{in} and a nozzle temperature of T, and meanwhile, to reproduce the continuous printing process, the nozzle domain travels at a print speed of V along the pre-defined printing path. The bottom surface is treated as the print bed, which allows heat transfer with the contact resin, and its temperature is 26.85 °C.

The feed speed is determined by matching the amount of extruded resin to the amount of printed resin. According to the scanning electron microscope (SEM) micrograph observed in the reference [46], the cross-section of the printed filament is assumed as a superellipse, as depicted in Fig. 3**B**. Consequently, the feed speed is calculated from mass conservation:

$$\pi R^2 V_{in} = V S_{superellipse}. \tag{3}$$

where, R is the nozzle radius, and $S_{superellipse}$ is the cross-section area of the printed filament, which is calculated through the Monte Carlo method.

The CFD model is defined to be a transient multiphase (air phase and PET-G phase) flow considering the influence of gravity, solidification, and melting. The volume of fluid method is utilised to capture the interface between air and PET-G. This model primarily focuses on the void-filling effect of the molten PET-G, ignoring the fibre effect and assuming the fluid density is constant. Additionally, the assumptions of incompressible fluid and laminar flow [42] are employed to describe the fluid flow, which satisfies the following equations:

Mass conservation

$$\nabla \cdot \mathbf{v} = 0. \tag{4}$$

Table 4: Fitting parameters of Carreau-WLF model for PET-G.

η_0	η_∞	λ_t	n	T_v	T_g
1530.23 Pa·s	0 Pa·s	0.03748 s	0.662	220 °C	80 °C

Momentum conservation

$$\frac{\partial}{\partial t}(\rho \mathbf{v}) + \nabla \cdot (\rho \mathbf{v}\mathbf{v}) = -\nabla p + \nabla \cdot \left[\eta \left(\nabla \mathbf{v} + \nabla \mathbf{v}^{\mathsf{T}}\right)\right] + \rho \mathbf{g} + \mathbf{f}(T^*) + \mathbf{F}_\sigma. \tag{5}$$

Energy conservation

$$\frac{\partial}{\partial t}\left[\rho c_p (T^* - T_{ref})\right] + \nabla \cdot \left[\rho c_p \mathbf{v} (T^* - T_{ref})\right] = \nabla \cdot (k \nabla T^*). \tag{6}$$

Where, $\mathbf{v}$ is the velocity vector of the fluid flow, ρ is density, t is time, p is pressure, η is viscosity, $\mathbf{g}$ is gravity vector, T^* is temperature, $\mathbf{f}(T^*)$ is a resistance source term which is used to simulate the solid state of PET-G by forcing its velocity to zero when polymer's temperature is below its solidification temperature, $\mathbf{F}_\sigma$ is the source term of surface tension, c_p is specific heat capacity, T_{ref} is the reference temperature (25 °C) where the system enthalpy is zero, k is the thermal conductivity. The material properties are summarised in Table 2.

The shear-dependent and temperature-dependent viscosity behaviour of PET-G is presented in Fig. 4. The viscosity of PET-G decreases as temperature and shear rate increase. With rising temperature, the rate of viscosity reduction gradually slows down. Conversely, with increasing shear rate, the rate of viscosity reduction gradually intensifies.

The Carreau-WLF model [42] was used to describe the dynamic viscosity behaviour η, as follows,

$$\eta = \eta_\infty + \frac{\eta_0 \alpha_T - \eta_\infty}{\left[1 + (\lambda_t \alpha_T \dot{\gamma})^2\right]^{\frac{1-n}{2}}}, \tag{7}$$

$$\ln \alpha_T = \frac{C_1 (T_v - T_g)}{C_2 + (T_v - T_g)} - \frac{C_1 (T^* - T_g)}{C_2 + (T^* - T_g)}, \tag{8}$$

where, η_0 represents the zero-shear rate viscosity; η_∞ is the infinite shear rate viscosity; $\dot{\gamma}$ the shear rate; λ_t the relaxation time; n the power law index; α_T the transforming factor; T^* the temperature corresponding to the viscosity predicted by the model; T_v the temperature corresponding to the viscosity that has been experimentally measured; T_g the glass transition temperature; C_1 and C_2 are constants where C_1 usually equals to 17.44, and C_2 equals to 51.6 K for polymers [42, 52]. We adopt 220 °C as the reference temperature (T_v) and use the shear rate-dependent viscosity data in 220 °C to fit the Carreau-WLF model. The fitting values are obtained in Table 4.

The experimental results of PET-G surface tension with varying temperatures are shown in Table 5. It was observed that surface tension plays a critical role in determining the final geometry of the printed structure. Specifically, variations in surface tension can lead to changes in strand morphology, layer adhesion, and void formation. As the temperature increases, the surface tension of PET-G decreases linearly from 37.10 to 35.13 mN/m. Combined with the viscosity results, it is evident that PET-G exhibits better flowability at higher temperatures.

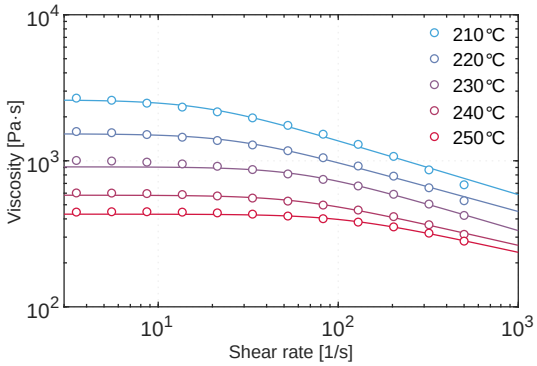


Figure 4: Shear rate- and temperature-dependent viscosity of PET-G. The data points are measured through rheometer and the curves are fitted using the Carreau model under different temperatures.

3.2.2. *Calculation of void content and mechanical properties*

To evaluate the relationship between the process parameters and the void content between the deposited filaments in the printed part, the void content was calculated based on the CFD results of the deposition process. As illustrated in Fig. 5, the void area was extracted from the middle zone of the simulated morphology, and the ratio of the void area to the middle zone area was taken as the void content. After obtaining the process-related void content information through the CFD model, the simulation strategy integrating the void content with the mechanical model is depicted in Fig. 5.

To verify the CFD model, we first established an RVE model to predict the equivalent material properties of the printed part, based on the void content, material properties of PET-G and carbon fibre prepreg, as well as their content ratios.

As illustrated in Fig. 5, the RVE consists of carbon fibre prepreg, PET-G, and voids. These three phases are randomly distributed within an RVE model with dimensions of $2\times 2\times 2\,\text{mm}^3$, based on their volume fractions in the printed parts. Finite element simulations are then performed to estimate the effective anisotropic properties of the printed parts. Among the three components, the carbon fibre prepreg exhibits anisotropic behaviour, with its elastic constants listed in Table 2. The PET-G is modelled as an isotropic material with an elastic modulus of 2.03 GPa and a Poisson's ratio of 0.368. The voids are assumed to have zero stiffness. The content of carbon fibre prepreg is 33.76%, which is determined based on the ratio of the fibre cross-sectional area to the cross-sectional area of the printed bead, as shown in Eq. (9). The void content is calculated from the CFD model.

$$V_{\text{Fibre content}} = \frac{\pi d^2}{4HL}, \tag{9}$$

where, d represents the fibre diameter (0.35 mm), H the hatch spacing (0.75 mm), and L the layer thickness (0.38 mm).

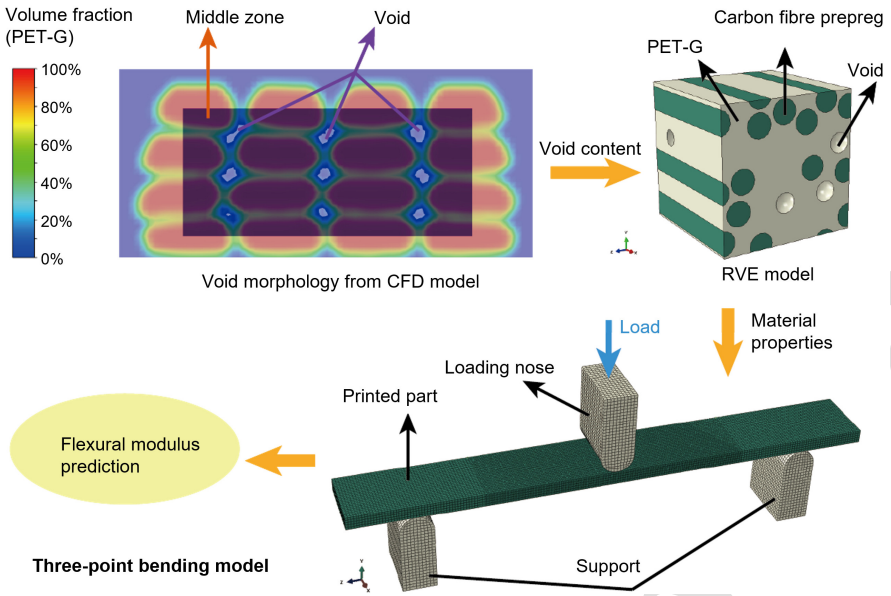


Figure 5: Simulation strategy integrating the void morphology with the mechanical model.

Table 5: Surface tension for PET-G under different nozzle temperatures.

Temp. [°C]	Surface tension 1 [mN/m]	Surface tension 2 [mN/m]	Surface tension 3 [mN/m]	AVG.	STD.	Density [g/cm^3]
250	35.04	35.22	35.13	35.13	0.07	1.193
240	36.42	36.51	36.31	36.41	0.08	1.229
230	37.46	37.46	36.65	37.19	0.38	1.244
220	36.29	36.55	36.71	36.52	0.17	1.214
210	37.77	36.65	36.98	37.13	0.47	1.196

Employing the finite element method (FEM), the RVE model underwent a 10% tensile and shear strain to calculate the equivalent material properties of the printed part. Subsequently, the obtained equivalent material properties were imported into a finite element model with dimensions of $80\times10\times2$ mm^3 (matching the size of the actual printed part). According to the ASTM D790-17 [53], a three-point bending simulation was performed to calculate the bending modulus, which was compared with the experimental data for validation.

4. Results

4.1. Temperature field results and analysis

The comparison of the experimental and numerical temperature profiles was conducted both spatially and temporally, allowing for a comprehensive analysis of their similarities and differences. Fig. 6**A** depicts the temperature profile at a specifically chosen location in the first layer for different nozzle temperatures. The mean absolute difference between the experimental and simulation data within the first 100 seconds since the respective deposition was 3.3, 3.7, and 4.5 °C at the nozzle temperature of 210, 230, and 250 °C, respectively. The comparison was made by linearly interpolating the numerical temperature at the experimental time spots and then making comparison. Despite the presence of minor deviations in the absolute values, there is considerable agreement between the numerical predictions and experimental results in terms of patterns and trends. Hence, the numerical thermal transfer model is validated by the experimental data. Following deposition, the local temperature experiences a rapid decrease from nozzle temperature (literally 210, 230, and 250 °C), which is then succeeded by a series of distinct peaks stemming from primary and secondary reheating processes. This kind of wave-like variation is also reported in [54], caused by the heat flow from the newly deposited upper layer neighbour. The cooling rate exerts a significant influence on the inter-layer bonding strength. As shown in Fig. 6**A**, these reheat temperature peaks, both experimentally recorded and numerically predicted, occur at closely matching intervals. The occurrence of a higher reheat peak temperature is attributed to an elevated nozzle temperature, while the cooling rates of different nozzle temperatures are similar. Especially shown in the enlarged view of the temperature profile of Fig. 6**A**, the primary highest cooling rate of experimental results is 7.70 °C/s and the simulation result is 16.71 °C/s. Besides, the presence of two distinct inter-layer reheating peaks also indicates a penetration depth spanning two layers. As the number of extruded layers increases, it can be observed that the deposition process of the composite material has a decreasing effect on the temperature profile. Upon comparison with experi-

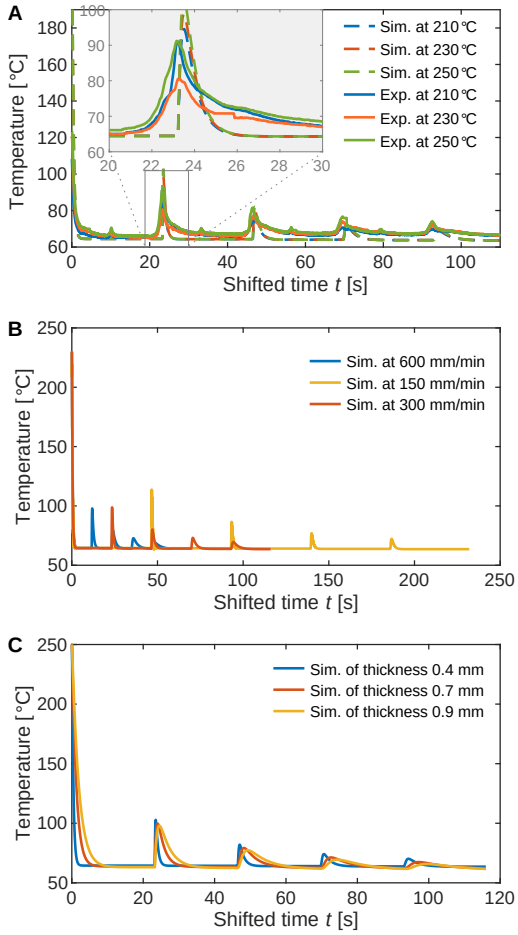


Figure 6: (**A**) Experimental and numerical results of temperature profile at different nozzle temperatures; (**B**) Numerical simulation results of temperature profile at different speeds; (**C**) Numerical simulation results of temperature profile at different layer thicknesses.

mental data, it is evident that the numerically computed cooling and heating rates are overestimation. The temperature peak sequences resulting from re-heating align precisely with the intra-layer and inter-layer time intervals for the specified location. The divergence between simulations and experiments, is due to the assumption of the numerical modelling (ideal cuboid voxel deposition), the variance in sampling frequencies between the experimental measurements and the numerical modelling, and boundary condition (e.g., the presence of hot closed chamber leads to low cooling rate). Further, the reheating period of experiments is longer than the simulation since the heat transfer model does not consider the contact area between the nozzle structure and deposited material. Fig. 6**B** shows the simulated temperature profile at a specifically chosen location in the first layer at different print speeds. In the simulation model, the temperature within the curve first starts from the set point temperature, and subsequently undergoes a dramatic drop, reverting to the print bed temperature. It indicates that heat transfer is independent of print speed. As the speed gradually increases, the printing time gradually decreases proportionally. Besides, as the material is extruded from the nozzle head, the peak value of repeated heating decreases with increasing print speed, as illustrated in the detailed enlarged views of the following re-heat peak of Fig. 6**B**. During printing, a slower print speed allows for more thorough heating inside the nozzle. A slower printing means a lower shear rate that increases the viscosity, provided that the temperature is constant. The cooling rate also gradually slows down. When the reheating temperature is lower than the glass transition temperature T_g, its effect on the interlayer bonding strength decreases.

In addition, considering that the glass transition is gradual and the interlayer bonding effect decreases exponentially with the shortening of the time in this temperature range, properly reducing the print speed can improve the interlayer bonding effect. Fig. 6**C** shows the simulated temperature profile at a specifically chosen location in the first layer under different layer thicknesses. It can be observed that variations in layer thickness significantly impact the sequence re-heating temperature and cooling rate. First, the volume of the composite material extruded per unit time also gradually increases as the layer thickness increases. Therefore, the peak of the secondary reheat temperature will gradually decrease as the layer thickness increases. As shown in the enlarged view of Fig. 6**C**, as the extruded material volume per unit time increases, the secondary reheating temperature decreases from 102.15 to 97.47 °C, and the cooling rate correspondingly drops from 69.31 to 6.71 °C/s.

Following these experiments and simulations, it was verified that the numerical model applies to CCF composites. Apart from previous aspects, another difference between the simulation and the experiment is that the start time of reheating is earlier than the predicted time since the established heat transfer model does not consider the impact of the nozzle structure on the printing process. However, for continuous fibre-reinforced composite printing, the extruded material is compacted by the nozzle, which is at the nozzle temperature. There is both convective and conductive heat transfer between the nozzle and the extruded material, resulting in a temperature profile that differs from that of pure resin printing. This will be optimised in the future to update the heat transfer model to include the conductive heat transfer from the nozzle to the adjacent strands. Moreover, based on the results, it can be observed that print speed and layer thickness have a more significant impact on thermal history than the nozzle temperature. Changes in print speed significantly affect the peak of reheating, while layer thickness has a more notable impact on the cooling rate. Therefore, it is anticipated that the inter and intra-layer coalescence of the interconnection will yield analogous effects.

4.2. Computational fluid dynamics analysis

During printing, process parameters such as nozzle temperature and print speed directly influence the thermal history evolution of the printed material, thereby affecting the flow behaviour of the resin, which would result in the varied void content in the printed part. Fig. 7 presents the cross-sections of printing morphology and the corresponding measurements of void content under the different combinations of process parameters. In it, Fig. 7**A** presents a line graph illustrating the void content after

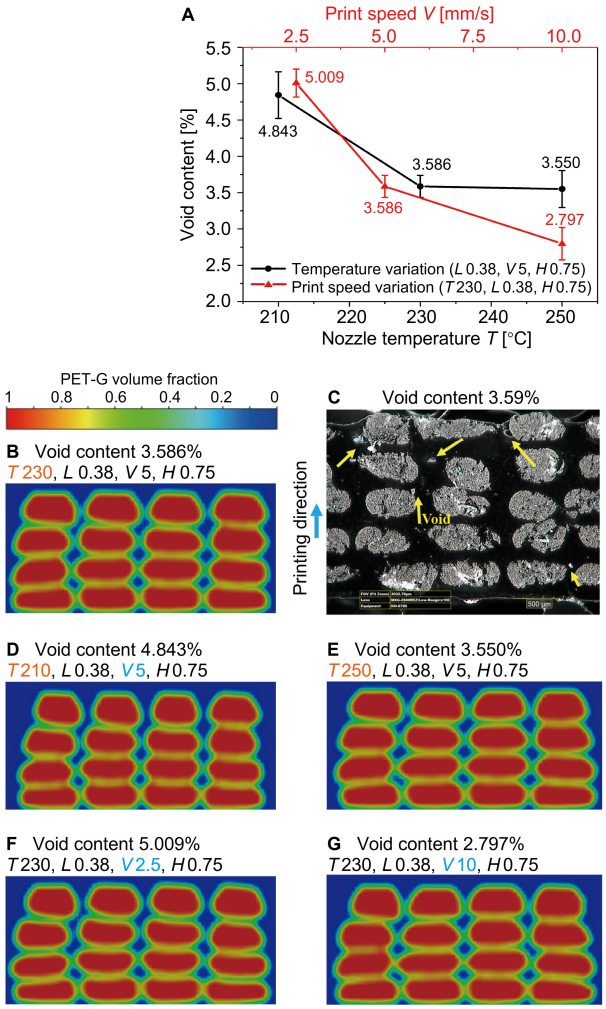


Figure 7: (**A**) The void content under different process parameters and (**B**-**G**) the corresponding cross-sections of the printing morphology: (**B**) simulation and (**C**) microscopic image under T 230, L 0.38, V 5, H 0.75; simulation under (**D**) T 210, L 0.38, V 5, H 0.75; (**E**) T 250, L 0.38, V 5, H 0.75; (**F**) T 230, L 0.38, V 2.5, H 0.75; (**G**) T 230, L 0.38, V 10, H 0.75.

multiple samples. The black line represents the relationship between the void content and nozzle temperature, while the red line depicts the relationship between the void content and print speed. Fig. 7**B**, **D**, and **E** illustrate the morphology changes as the nozzle temperature increases from 210 to 250 °C, while Fig. 7**B**, **F**, and **G** show the morphology changes as the print speed increases from 2.5 to 10 mm/s. To validate the effectiveness of the model, we scanned the printed part under the process parameters of T 230, L 0.38, V 5, H 0.75 and obtained the microscopic image as shown in Fig. 7**C**. The void content measured from this micro-CT analysis is 3.59% and the corresponding void content predicted from the CFD model is 3.586%, which verifies the feasibility of the CFD model. Additionally, following the method in Section 3.2.2, we modified the RVE model based on the predicted void content under the process parameters T 230, L 0.38, V 5, H 0.75. This modified model was then used to estimate the flexural modulus of the printed part. The predicted flexural modulus of the printed part is 39.39 GPa, while the experimental result is 30.34 (±0.59) GPa (Please find the detailed experimental data in our previous work [11]).

The overestimation of the flexural modulus is mainly due to three factors. First, other defects are not considered. This study focuses on the relationship between the printing process and the inter-bead void defects. However, during the printing of CFRC, there are many defect types associated with the printing process that also weaken the mechanical properties of the printed part. For example, the weak interface in the actual printed part reduces the stress transfer efficiency between the fibres and the resin, preventing the fibres from effectively sharing the load. This leads to premature fibre failure at stress concentration points, causing the experimentally measured mechanical properties to be lower than the predicted values. Second, mismatch void morphology between model and reality. The RVE model used in this study estimates the material properties by assuming spherical voids to account for the void content. However, as shown in Fig. 7, the actual void morphology is complex, and this inconsistency in void shape may be a reason for the estimation bias. Third, actual defects are not considered in the three-point bending model. This study uses the RVE to estimate the overall material properties of the printed part and applies a defect-free three-point bending model to predict the bending modulus. However, the actual printed part may fail prematurely at stress concentration points due to defects when subjected to loading. This also contributes to the predicted values being higher than the actual ones.

Depicted in Fig. 7**B**, **D**, and **E**, as the nozzle temperature increases from 210 to 250 °C, the void content decreases from 4.843% to 3.550%. This phenomenon can be attributed to three main reasons. Firstly, the higher nozzle temperature reduces the viscosity of the extruded resin, which enhances its flow capability and makes the extruded resin flow more easily into the gaps between the filaments, thereby effectively filling them. Secondly, the elevated nozzle temperature allows the resin to remain in the molten state for longer periods, which increases its flow duration to fill the void. Lastly, the higher nozzle temperature promotes more quick and extensive remelting of the adjacent previously deposited resin, which would resume flowing to continue filling the adjacent voids. These factors collectively contribute to the reduced void content in the printed parts at higher nozzle temperatures.

It is noted that this high-temperature effect gradually diminishes with the increasing nozzle temperature, primarily because the reduction effect of high temperature on reducing the resin viscosity decreases with the elevating temperature, as presented in the viscosity curves of PET-G (Fig. 4). Thus, as the nozzle temperature increases from 210 to 230 °C, the void content decreases from 4.843% to 3.586%, while within the same temperature range, from 230 to 250 °C, the void content remains essentially unchanged with a variation of 0.036%. The contribution of temperature to the void content becomes limited when the nozzle temperature exceeds 230 °C.

Depicted in Fig. 7**B**, **F**, and **G**, as the print speed elevates from 2.5 to 10 mm/s, the void content reduces from 5.009% to 2.797%. This phenomenon can be attributed to two main

Journal Pre-proof

Journal Pre-proof

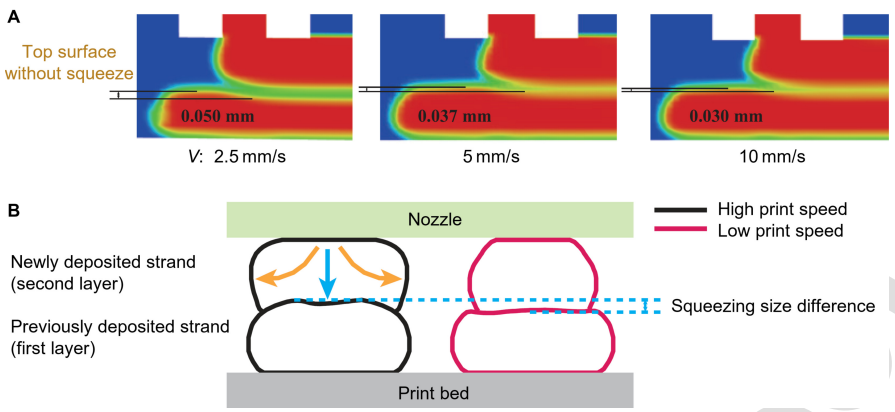


Figure 8: (**A**) Squeezing size of the previous layer under different print speeds; (**B**) A diagram of the deposited strand flow under low and high print speeds.

reasons. On one hand, at high print speeds, the heat of the molten resin struggles to transfer efficiently to the resin previously deposited, resulting in less resin being remelted. Consequently, the squeezing effect of the molten resin on the previous layer diminishes with the elevated print speed. As illustrated in Fig. 8**A**, increasing the print speed from 2.5 to 10 mm/s reduces the squeezing size of the previous layer from 0.05 to 0.03 mm. As a result, as shown in Fig. 8**B**, at high print speeds, the newly deposited strand would squeeze more lightly on the previous layer (first layer), reducing the height available for the second layer compared to low print speeds. Given the constant amount of the extruded resin per unit length and the fixed height of the two layers, the newly deposited strand is more constrained vertically at high print speeds, causing it to flow laterally to fill voids.

On the other hand, the shear rate increases with the elevating print speed, which would cause a decrease in the molten resin viscosity. This means that the newly deposited strand flows with less resistance at high print speeds, making it easier to flow laterally and fill voids. Consequently, increasing the print speed leads to a decrease in the void content.

5. Discussion

The influence of process parameters on the thermal history and interfacial behaviour of FFF-printed CFRCs have been investigated in previous sections. Considering the fact FFF is temperature-based process, process parameters will determine the thermal history which directly affects material properties. Consequently, the thermal history is a crucial link to clarify the coupled effects of process parameters on microstructure and interfacial formation, and establishing the correlation between the thermal history and interfacial properties is necessary.

5.1. Flow behaviour and the void defect formation

Based on the thermal history observed during the printing process in Section 4.1, it is evident that process parameters are closely linked to the thermal history. As the nozzle temperature increases, the print speed reduces, and the layer thickness decreases, the material being printed is exposed to more heat, promoting better sintering between the printed strands. Additionally, under low speed, high temperature, and thin layer conditions, the accumulated heat is more effectively transferred to the previously printed layers, enhancing the secondary bonding at the interlayer interfaces and thereby improving the overall performance of the printed part. A similar trend was observed in the CFD results discussed in Section 4.2. As the nozzle temperature increases, the resin viscosity decreases, allowing the resin to flow more easily into voids and fill them. This phenomenon is well illustrated by the results in Fig. 7, where the void content decreases with rising temperature. Additionally, at a given nozzle temperature, a higher print speed reduces the compressive effect of the printed strand on the previous layer, which facilitates the flow of the printed strand in the current layer to fill voids. It is important to emphasize that the insufficient heat accumulation caused by high-speed printing would prevent adequate healing between layers, leading to a deterioration in the performance of the printed part. Therefore, high-speed printing is a double-edged sword. When optimizing the print speed, it is crucial to balance the trade-off between the low void content and reduced interfacial bonding strength. Furthermore, the relationship between high-speed printing and void content is based on the assumption of sufficient resin extrusion. In actual printing, due to the limitation of resin melting speed, there is a correlation between resin extrusion amount and print speed. This is another factor that needs to be considered when optimizing the print speed. Section 5.2 provides a detailed discussion of their relationship and potential improvements.

Furthermore, the CFD model could provide explanations of the impact of process parameters on the microstructure and flow characteristics of the printed strand from a fluid dynamics perspective. Fig. 9 presents the CFD simulation visualization of the overall printing morphology (Fig. 9**A**) and the local cross-section with typical stages of strand shapes (Fig. 9**B**-**F**). Fig. 9**C** depicts the cross-section of the first printed filament along with its resin streamlines. As the molten resin flows out from the nozzle, it spreads to both sides of the printing path due to the resin extrusion velocity and the nozzle pressure, without inter-

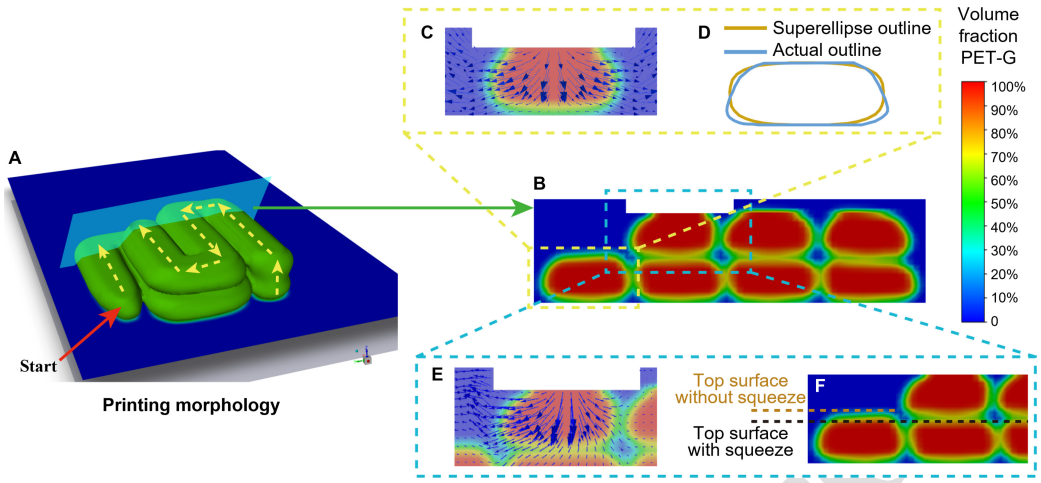


Figure 9: The CFD simulation visualisation of (**A**) printing morphology and (**B**-**F**) typical stages of strand shapes: (**B**) the cross-section of the printed part; (**C**) the streamline line of the first deposited strand; (**D**) the ideal and actual outline of strand shape without other strand influence; (**E**) the streamline line of a newly deposited strand; and (**F**) the illustration of the squeeze effect by deposited strand.

ference from other strands. Moreover, because of the combined effects of the extrusion velocity and gravity, the molten resin tends to flow downward, resulting in a strand shape that is narrower at the top and wider at the bottom after deposition. It is important to note that the amount of resin extruded from the nozzle is set under the ideal condition, meaning that the strands with a super-ellipse profile just touch each other. However, the actual shape of this strand, being narrower at the top and wider at the bottom, results in the width at its widest part exceeding the set hatch spacing (as shown in Fig. 9**D**), leading to the printed strand deviating from the intended geometric positions. Moreover, as shown in Fig. 9**A**, the molten resin moves along the printing path indicated by the yellow arrow. As the nozzle moves away, the temperature of the deposited resin gradually decreases and it transitions from liquid to solid. Subsequently, when the nozzle moves back to the vicinity of the previously deposited resin, the newly deposited resin transfers heat to the adjacent solidified resin, causing its contact area to melt again. During this process, the polymer chains of the previously deposited resin and the newly deposited resin would entangle, forming an interface that enables stress transfer between the printed filaments when the printed part is under compaction.

For each strand on the same layer, the newly deposited resin tends to flow laterally as shown in Fig. 9**C**. However, as aforementioned, the actual width of the deposited strand exceeds the set hatch spacing, causing the previously deposited strand to encroach on the space meant for the subsequent strands. Due to the space encroachment by the previously deposited strands, the newly deposited resin could only flow towards the side without deposited strands, as shown in Fig. 9**B** and **E**. This results in the entire layer of strands deviating from the designed positions (also found in [46]), and this offset error would gradually accumulate as printing continues, negatively affecting the geometric accuracy and void control of the printed part.

For strands in different layers, the newly deposited strand would melt the upper surface of the strand deposited in the previous layer. Due to the gravitational force and extrusion velocity of the newly deposited resin, the previously deposited strand would be squeezed, thereby reducing its layer thickness (Fig. 9**F**). This also harms the geometric accuracy of the printed part. More critically, this negative effect accumulates as the number of printed layers increases. Fig. 10**B** demonstrates how the void content of the printed part changes when printing two, three, and four layers, clearly indicating that as the layer count grows, the porosity increases from 2.153% to 3.586%. Therefore, in future studies, it is essential to account for how process parameters affect thermal history and flow behaviour, and optimize the process parameters for each layer using the simulation results. Moreover, for manufacturing equipment development and process optimisation, our analysis of the FFF forming mechanism and thermal history informs extrusion system design, nozzle temperature control, and interlayer bonding strategies, while the CFD-thermal modelling framework supports predictive, data-driven tuning of key parameters like printing speed and layer height. In structural design, our physics-informed model links processing conditions to mechanical properties, enabling designers to optimise part geometry and loading direction early on, reducing trial-and-error and supporting virtual testing.

5.2. Limitation and outlook

As mentioned in Section 4.2, we have also identified a discrepancy between simulations and experiments, that parts printed at lower speeds generally demonstrate stronger mechanical properties. This discrepancy can be attributed to two primary reasons. On one hand, because FFF involves the resin melting process, an excessively high print speed may result in the resin melting rate failing to keep up with the print speed. Furthermore, at high printing speeds, the residence time of the resin within the nozzle is short, resulting in insufficient and uneven heating. As a consequence, the resin does not fully melt, and the mobility of molecular chains is limited, leading to weak

Journal Pre-proof

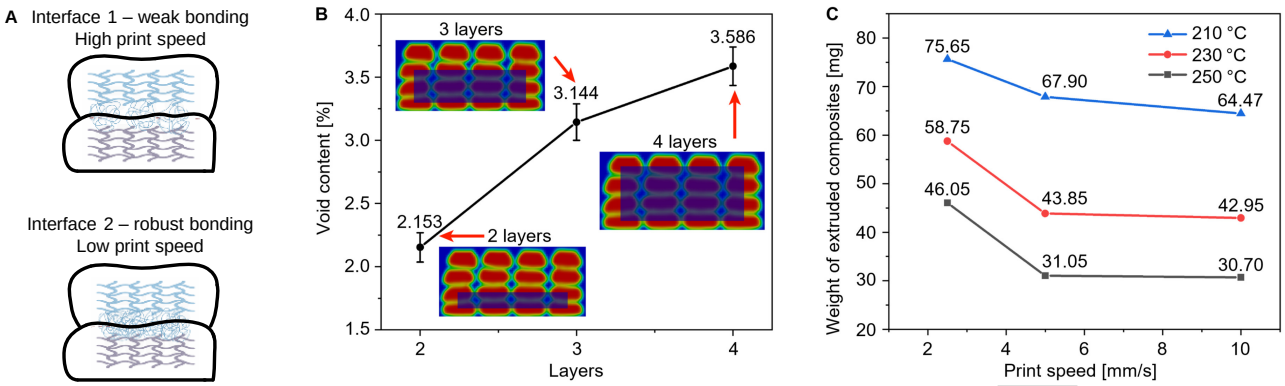


Figure 10: (**A**) The connection between incomplete resin melting and interfacial defects; (**B**) The void content under different printing layers; (**C**) The influences of nozzle temperature and print speed on the quality of single printed CFRCs.

interfacial bonding and the formation of interfacial defects, as shown in Fig. 10**A**. In contrast, at lower printing speeds, the resin remains in the nozzle for a longer duration, allowing for more uniform heating and complete melting. The reduced printing speed enhances interfacial strength by increasing polymer chain mobility, which facilitates mechanical interlocking and promotes robust interfacial bonding. However, the amount of extrusion resin in the CFD simulation is set ideally to fulfil the demands for fast printing. On the other hand, our study focuses on the correlation between process parameters and void content. Although the high print speed is beneficial for reducing void at the assumption of an ideal amount of extrusion resin, the mechanical properties of the printed parts are influenced not only by the void content but also significantly by the interfacial strength, which determines the stress transmission efficiency. In the situation of high print speed, the healing time is too short to achieve good bonding between the printed strands. This weakened interface, induced by the high print speed, would cause a severe decline in the mechanical properties. To enhance it, we printed individual strands at different print speeds and temperatures, and subsequently weighed them. The theoretical weight for each strand is 0.0565 g. As shown in Fig. 10**C**, the experiments demonstrate that the quality of the single printed CFRP filament deviates from the theoretical value under the various combinations of nozzle temperature and print speed.

Based on the results, it was found that the amount of extruded resin gradually decreases with the increase in temperature and print speed. These results validate our hypothesis. Besides, the increase in print speed and nozzle temperature can reduce the resin viscosity, which diminishes the adhesion effect of viscous resin, as depicted in Fig. 10**C**. The established CFD model does not account for these factors, as it assumes that the resin is extruded from the nozzle at the expected resin feed rate. This discrepancy is one of the reasons why the experimental results do not fully correspond to the simulation outcomes. Therefore, we will enhance our CFD model presented in this paper in future research to explore the relationship between this dragging effect and process parameters, as well as its implications for the printing performance.

The core idea is to consider the varying flow behaviour of molten resin when extruded from the nozzle, building upon the current model. Here are two viable approaches to optimize the CFD model. The first approach is to develop an integrated CFD model for both the intra-nozzle and the deposition process. The current model only simulates the deposition process, simplifying the material behaviour in the nozzle by assuming that the initial temperature and flow behaviour of the extruded resin are constant. In the future, we will develop a intra-nozzle CFD model that can reveal the impact of printing parameters on the resin flow inside the nozzle. This will be further coupled with the existing deposition CFD model, using the simulated extrusion state as input for the deposition model, thus enabling a comprehensive analysis of the printing process. The challenge of this approach lies in establishing the information exchange interface between the intra-nozzle CFD model and the deposition CFD model. Additionally, this approach will significantly increase computational demands. One possible way to improve computational efficiency might be to build a physics-based neural network model based on the simulation results. The second approach involves designing a specialized fluid measurement device based on the nozzle structure, paired with advanced visual technologies to measure the flow rate and temperature of the extruded resin under different printing parameter combinations. These data will serve as inputs for the existing deposition CFD model. This approach provides real physical information, but due to current experimental limitations, it can only yield partial resin melt data. Details such as flow direction are difficult to obtain.

6. Conclusions

The FFF printing process of CFRCs relies on material extrusion, where temperature plays a crucial role in ensuring that the extruded material is properly liquefied, allowing for unobstructed flow through the nozzle and subsequent adhesion to the previous layer. To validate this process, a heat transfer model and a CFD model are developed to demonstrate the correlation between thermal history and interfacial performance. By comparing simulation results with experimental data, the maximum

mean absolute difference of the material temperature variation is 4.5 °C, and the flexural modulus error is less than 29.8%, confirming the validity of the models. Additionally, through in-depth analysis, we have gained substantial insights into the FFF printing process of continuous carbon fibre-reinforced composites:

(1) Through modelling and analysis, it is observed that appropriately increasing the nozzle temperature can enhance the flowability and flow duration of the deposited resin, facilitating the interfacial healing of previously deposited strands and reducing voids during the printing process. Compared to nozzle temperature, print speed and layer thickness have a significant impact on reheat peak and cooling time. Similarly, our CFD model also reveals these effects, which further influence the formation of porosity and interfacial bonding. Moreover, it was found that the amount of extruded resin during printing is closely related to the print speed, leading to discrepancies between simulation results and experimental findings. These discrepancies can be addressed by coupling the flow simulation of the deposition process with the in-nozzle processes to improve accuracy.

(2) Due to the influence of process parameters on resin speed and flowability, the actual hatch spacing and layer thickness deviate from the design values. The resulting porosity and microstructure, caused by these deviations, accumulate with each printed layer, negatively impacting the final structure's dimensions, surface accuracy, and defect control. Therefore, it is necessary to adjust the process parameters in real-time based on the conditions of the previously printed layer. Further exploration is required to precisely control the thermal history of the extruded material, understand its correlation with process parameters, and achieve optimal cross-sectional shape and interlayer adhesion. This will allow for timely compensation for any defects, thus preventing the accumulation of these effects.

(3) The findings of this study can guide the manufacturing of high-quality composite structures by revealing the relationship between the thermal history influenced by process parameters and the interfacial performance in CFRCs extrusion-based FFF. To ultimately promote the adoption of CFRCs parts manufactured by FFF in practical engineering applications, future research will focus on optimizing existing CFD models and proposing online real-time compensation strategies. For instance, the local temperature can theoretically be monitored in real-time and used to adjust parameters for improved bonding, such as by applying laser-based preheating or post-heating.

(4) With increasing composite complexity, fast and accurate process models are essential for advancing smart manufacturing of aerial vehicles or satellites in practical applications. These models help explore optimal strategies across varying equipment, materials, and designs, offering low-cost insights into processing mechanisms. When combined with data-driven algorithms, they enable real-time prediction and control, supporting digital twin technologies for efficient, high-quality production. This approach reduces reliance on trial-and-error, enhances process understanding, and accelerates the adoption of composites across industries by enabling intelligent, continuous, and optimised manufacturing workflows.

Data availability statement

The data are available from the authors upon request.

Acknowledgements

This work is supported by National Natural Science Foundation of China (Grant No. 52205003), the China Scholarship Council program, Research Foundation of China Academy of Railway Sciences Corporation Limited (2022YJ320). J.Z. acknowledges the Fonds Wetenschappelijk Onderzoek – Vlaanderen (FWO) for the junior postdoctoral fellowship (Grant No. 12B3B24N). The authors would like to acknowledge Loren De Vogelaer and Fankai Meng for their technical support.

References

[1] B. Fedulov, A. Fedorenko, A. Khaziev, F. Antonov, Optimization of parts manufactured using continuous fiber three-dimensional printing technology, *Composites Part B: Engineering* 227 (**2021**) 109406. doi:10.1016/j.compositesb.2021.109406.

[2] L. Zhou, J. Fu, Y. He, A review of 3D printing technologies for soft polymer materials, *Advanced Functional Materials* 30 (**2020**) 2000187. doi:10.1002/adfm.202000187.

[3] P. Zhuo, S. Li, I. A. Ashcroft, A. I. Jones, Material extrusion additive manufacturing of continuous fibre reinforced polymer matrix composites: A review and outlook, *Composites Part B: Engineering* 224 (**2021**) 109143. doi:10.1016/j.compositesb.2021.109143.

[4] S. K. Eshkalak, E. R. Ghomi, Y. Dai, D. Choudhury, S. Ramakrishna, The role of three-dimensional printing in healthcare and medicine, *Materials and Design* 194 (**2020**) 108940. doi:10.1016/j.matdes.2020.108940.

[5] K. Osouli-Bostanabad, T. Masalehdan, R. M. I. Kapsa, A. Quigley, A. Lalatsa, K. F. Bruggeman, S. J. Franks, R. J. Williams, D. R. Nisbet, Traction of 3D and 4D printing in the healthcare industry: from drug delivery and analysis to regenerative medicine, *ACS Biomaterials Science & Engineering* 8 (**2022**) 2764–2797. doi:10.1021/acsbiomaterials.2c00094.

[6] S. El-Sayegh, L. Romdhane, S. Manjikian, A critical review of 3D printing in construction: benefits, challenges, and risks, *Archives of Civil and Mechanical Engineering* 20 (**2020**) 1–25. doi:10.1007/s43452-020-00038-w.

[7] L. Li, W. Liu, Y. Wang, Z. Zhao, Mechanical performance and damage monitoring of CFRP thermoplastic laminates with an open hole repaired by 3D printed patches, *Composite Structures* 303 (**2023**) 116308. doi:10.1016/j.compstruct.2022.116308.

[8] S. C. Altıparmak, V. A. Yardley, Z. Shi, J. Lin, Extrusion-based additive manufacturing technologies: State of the art and future perspectives, *Journal of Manufacturing Processes* 83 (**2022**) 607–636. doi:10.1016/j.jmapro.2022.09.032.

[9] J. Zhang, B. Van Hooreweder, E. Ferraris, Fused filament fabrication on the Moon, *JOM* 74 (**2022**) 1111–1119. doi:10.1007/s11837-021-05031-z.

[10] F. Liu, S. Wang, W. Zhang, X. Ding, E. Ferraris, J. Ivens, Mechanical and interfacial analysis of 3D-printed two-matrix continuous carbon fibre composites for enhanced structural performance, *Composites Part A: Applied Science and Manufacturing* 178 (**2024**) 108105. doi:10.1016/j.compositesa.2024.108105.

[11] F. Liu, E. Ferraris, J. Ivens, Mechanical investigation and microstructure performance of a two-matrix continuous carbon fibre composite fabricated by 3D printing, *Journal of Manufacturing Processes* 79 (**2022**) 383–393. doi:10.1016/j.jmapro.2022.04.050.

[12] H. Kong, P. Qu, , X. Li, D. Kong, A. Guo, S. Wang, Y. Wan, T. J., An investigation into mechanical properties of a 3D printed two-matrix continuous fiber composites with multi-cavity structure, *Journal of Materials Research and Technology* 26 (**2023**) 4365–4386. doi:10.1016/j.jmrt.2023.08.132.

Journal Pre-proof

[13] V. V. Vasil'ev, V. A. Salov, Development and examination of a two-matrix glassfiber composite with high transverse strain, *Mechanics of Composite Materials* 20 (**1985**) 463–467. doi:10.1007/BF00609647.

[14] A. V. Azarov, F. K. Antonov, V. V. Vasil'ev, M. V. Golubev, D. S. Krasovskii, A. F. Razin, V. A. Salov, V. V. Stupnikov, A. R. Khaziev, Development of a two-matrix composite material fabricated by 3D printing, *Polymer Science Series D* 10 (**2017**) 87–90. doi:10.1134/S1995421217010026.

[15] T. Li, X. Du, D. Zhou, Y. Mao, R. Tao, D. Fang, Research on foldable two-matrix 3D braided composites: Manufacturing and bending progressive damage, *Composites Science and Technology* 255 (**2024**) 110637. doi:10.1016/j.compscitech.2024.110637.

[16] L. Mazzocchetti, T. Benelli, E. D'Angelo, C. Leonardi, G. Zattini, L. Giorgini, Validation of carbon fibers recycling by pyro-gasification: The influence of oxidation conditions to obtain clean fibers and promote fiber/matrix adhesion in epoxy composites, *Composites Part A: Applied Science and Manufacturing* 112 (**2018**) 504–514. doi:10.1016/j.compositesa.2018.07.007.

[17] M. Iragi, C. Pascual-González, A. Esnaola, C. S. Lopes, L. Aretxabaleta, Ply and interlaminar behaviours of 3D printed continuous carbon fibre-reinforced thermoplastic laminates; effects of processing conditions and microstructure, *Additive Manufacturing* 30 (**2019**) 100884. doi:10.1016/j.addma.2019.100884.

[18] S. O. Obadimu, A. Kasha, K. I. Kourousis, Tensile performance and plastic anisotropy of material extrusion steel 316L: Influence of primary manufacturing parameters, *Additive Manufacturing* 60 (**2022**) 103297. doi:10.1016/j.addma.2022.103297.

[19] R. S. Mutyala, K. Park, E. E. Günay, G. Kim, S. Lau, J. Jackman, G. E. O. Kremer, Effect of FFF process parameters on mechanical strength of CFR-PEEK outputs, *International Journal on Interactive Design and Manufacturing* 16 (**2022**) 1385–1396. doi:10.1007/s12008-022-00944-8.

[20] Y. Ming, S. Zhang, W. Han, B. Wang, Y. Duan, H. Xiao, Investigation on process parameters of 3D printed continuous carbon fiber-reinforced thermosetting epoxy composites, *Additive Manufacturing* 33 (**2020**) 101184. doi:10.1016/j.addma.2020.101184.

[21] Z. Zhang, Y. Long, Z. Yang, K. Fu, Y. Li, An investigation into printing pressure of 3D printed continuous carbon fiber reinforced composites, *Composites Part A: Applied Science and Manufacturing* 162 (**2022**) 107162. doi:10.1016/j.compositesa.2022.107162.

[22] X. Gao, S. Qi, X. Kuang, Y. Su, J. Li, D. Wang, Fused filament fabrication of polymer materials: A review of interlayer bond, *Additive Manufacturing* 37 (**2021**) 101658. doi:10.1016/j.addma.2020.101658.

[23] K. Saeed, A. McIlhagger, E. Harkin-Jones, C. McGarrigle, D. Dixon, M. A. Shar, A. McMillan, E. Archer, Characterization of continuous carbon fibre reinforced 3D printed polymer composites with varying fibre volume fractions, *Composite Structures* 282 (**2022**) 115033. doi:10.1016/j.compstruct.2021.115033.

[24] F. Caltanissetta, G. Dreifus, A. J. Hart, B. M. Colosimo, In-situ monitoring of material extrusion processes via thermal videoimaging with application to big area additive manufacturing (BAAM), *Additive Manufacturing* 58 (**2022**) 102995. doi:10.1016/j.addma.2022.102995.

[25] O. Holzmond, X. Li, In situ real time defect detection of 3D printed parts, *Additive Manufacturing* 17 (**2017**) 135–142. doi:https://doi.org/10.1016/j.addma.2017.08.003.

[26] R. Badarinath, V. Prabhu, Real-time sensing of output polymer flow temperature and volumetric flowrate in fused filament fabrication process, *Materials* 15 (2) (**2022**). doi:10.3390/ma15020618.

[27] L. Li, R. McGuan, R. Isaac, P. Kavehpour, R. Candler, Improving precision of material extrusion 3D printing by in-situ monitoring & predicting 3D geometric deviation using conditional adversarial networks, *Additive Manufacturing* 38 (**2021**) 101695. doi:10.1016/j.addma.2020.101695.

[28] M. Moretti, A. Rossi, N. Senin, In-process monitoring of part geometry in fused filament fabrication using computer vision and digital twins, *Additive Manufacturing* 37 (**2021**) 101609. doi:10.1016/j.addma.2020.101609.

[29] D. Yang, H. Zhang, J. Wu, E. D. McCarthy, Fibre flow and void formation in 3D printing of short-fibre reinforced thermoplastic composites: An experimental benchmark exercise, *Additive Manufacturing* 37 (**2021**) 101686. doi:10.1016/j.addma.2020.101686.

[30] J. Zhang, W. Yang, Y. Li, Process-dependent multiscale modeling for 3D printing of continuous fiber-reinforced composites, *Additive Manufacturing* 73 (**2023**) 103680. doi:10.1016/j.addma.2023.103680.

[31] D. D. Phan, J. S. Horner, Z. R. Swain, A. N. Beris, M. E. Mackay, Computational fluid dynamics simulation of the melting process in the fused filament fabrication additive manufacturing technique, *Additive Manufacturing* 33 (**2020**) 101161. doi:10.1016/j.addma.2020.101161.

[32] S. Miri, J. Rana, K. Fayazbakhsh, C. Ghnatios, Numerical and experimental study of the consolidation of continuous carbon fiber thermoplastics made by robotic 3D printing, *International Journal of Material Forming* 18 (1) (**2024**). doi:10.1007/s12289-024-01865-5.

[33] Y. Fu, X. Yao, Multi-scale analysis for 3D printed continuous fiber reinforced thermoplastic composites, *Composites Science and Technology* 216 (**2021**) 109065. doi:10.1016/j.compscitech.2021.109065.

[34] D. Yang, K. Wu, L. Wan, Y. Sheng, A particle element approach for modelling the 3D printing process of fibre reinforced polymer composites, *Journal of Manufacturing and Materials Processing* 1 (**2017**) 10. doi:10.3390/jmmp1010010.

[35] R. Comminal, M. P. Serdeczny, D. B. Pedersen, J. Spangenberg, Numerical modeling of the strand deposition flow in extrusion-based additive manufacturing, *Additive Manufacturing* 20 (**2018**) 68–76. doi:10.1016/j.addma.2017.12.013.

[36] H. Xia, J. Lu, G. Tryggvason, A numerical study of the effect of viscoelastic stresses in fused filament fabrication, *Computer Methods in Applied Mechanics and Engineering* 346 (**2019**) 242–259. doi:10.1016/j.cma.2018.11.031.

[37] C. Ghnatios, K. Fayazbakhsh, Warping estimation of continuous fiber-reinforced composites made by robotic 3D printing, *Additive Manufacturing* 55 (**2022**) 102796. doi:10.1016/j.addma.2022.102796.

[38] F. Wang, G. Wang, F. Ning, Z. Zhang, Fiber–matrix impregnation behavior during additive manufacturing of continuous carbon fiber reinforced polylactic acid composites, *Additive Manufacturing* 37 (**2021**) 101661. doi:10.1016/j.addma.2020.101661.

[39] Q. Sun, G. M. Rizvi, C. T. Bellehumeur, P. Gu, Effect of processing conditions on the bonding quality of FDM polymer filaments, *Rapid Prototyping Journal* 14 (**2008**) 72–80. doi:10.1108/13552540810862028.

[40] M. Faes, E. Ferraris, D. Moens, Influence of inter-layer cooling time on the quasi-static properties of ABS components produced via fused deposition modelling, *Procedia CIRP* 42 (**2016**) 748–753. doi:10.1016/j.procir.2016.02.313.

[41] S. Simaafrookhteh, P. Tsokanas, T. Loutas, S. V. Lomov, J. Ivens, Measuring the interlaminar fracture toughness of thin carbon fiber/polyamide6 composites using adhesively bonded stiffeners, *Composites Part A: Applied Science and Manufacturing* 176 (**2024**) 107841. doi:10.1016/j.compositesa.2023.107841.

[42] J. Du, Z. Wei, X. Wang, J. Wang, Z. Chen, An improved fused deposition modeling process for forming large-size thin-walled parts, *Journal of Materials Processing Technology* 234 (**2016**) 332–341. doi:10.1016/j.jmatprotec.2016.04.005.

[43] ASTM D7605-11(2022): Standard test method for thermoplastic elastomers—measurement of polymer melt rheological properties and congealed dynamic properties using rotorless shear rheometers (**2022**). doi:10.1520/D7605-11R22.

[44] J. Zhang, B. Van Hooreweder, E. Ferraris, T4F3: Temperature for Fused Filament Fabrication, *Progress in Additive Manufacturing* 7 (**2022**) 971–991. doi:10.1007/s40964-022-00271-0.

[45] H. Prajapati, D. Ravoori, A. Jain, Measurement and modeling of filament temperature distribution in the standoff gap between nozzle and bed in polymer-based additive manufacturing, *Additive Manufacturing* 24 (**2018**) 407–413. doi:10.1016/j.addma.2018.09.030.

[46] J. Y. Wang, D. D. Xu, W. Sun, S. M. Du, J. J. Guo, G. J. Xu, Effects of nozzle-bed distance on the surface quality and mechanical properties of fused filament fabrication parts, *IOP Conference Series: Materials Science and Engineering* 479 (**2019**) 012094. doi:10.1088/1757-899X/479/1/012094.

[47] PETG Biocide - material description, print settings, and properties, https://rec3d.ru/rec-wiki/, accessed: 2021-02-18.

[48] S. Bard, F. Schönl, M. Demleitner, V. Altstädt, Influence of fiber volume content on thermal conductivity in transverse and fiber direction of carbon fiber-reinforced epoxy laminates, *Materials* 12 (**2019**) 1084. doi:10.3390/ma12071084.

Journal Pre-proof

[49] ANSYS Fluent - CFD Software, http://www.ansys.com/products/fluids/ansys-fluent (**2016**).

[50] S. Valvez, A. P. Silva, P. N. B. Reis, Optimization of printing parameters to maximize the mechanical properties of 3D-printed PETG-based parts, *Polymers* 14 (**2022**) 2564. doi:10.3390/polym14132564.

[51] J. Zhang, E. Vasiliauskaite, A. De Kuyper, C. De Schryver, F. Vogeler, F. Desplentere, E. Ferraris, Temperature analyses in fused filament fabrication: from filament entering the hot-end to the printed parts, *3D Printing and Additive Manufacturing* 9 (2) (**2022**) 132–142. doi:10.1089/3dp.2020.0339.

[52] T. Osswald, N. Rudolph, Polymer rheology, Carl Hanser, München, **2015**.

[53] ASTM D790-17: Standard test methods for flexural properties of unreinforced and reinforced plastics and electrical insulating materials (**2017**). doi:10.1520/D0790-17.

[54] C. Kousiatza, D. Karalekas, In-situ monitoring of strain and temperature distributions during fused deposition modeling process, *Materials and Design* 97 (**2016**) 400–406. doi:10.1016/j.matdes.2016.02.099.

Journal Pre-proof

Journal Pre-proof

Highlight

A numerical thermal transfer model and computational fluid dynamic model are developed to understand the impact of thermal history on FFF printing process

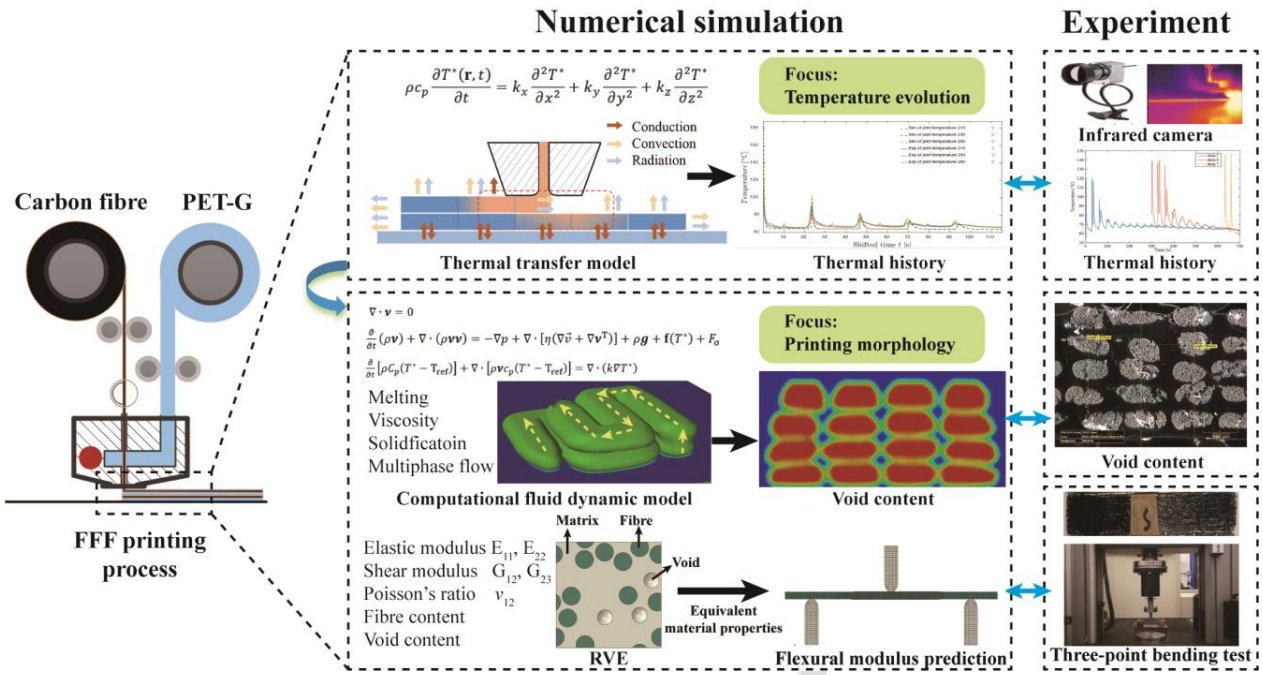
Print speed and layer thickness have a remarkable impact on the reheat peak and cooling time

Moderately increasing the nozzle temperature can enhance the flowability and flow duration of the deposited resin, thereby promoting interfacial healing

The actual hatch spacing of the strand is largely influenced by the resin flowability related to temperature, shear rate, and surface tension

Journal Pre-proof

Graphical Abstract



Journal Pre-proof

Journal Pre-proof

Declaration of interests

☒ The authors declare that they have no known competing financial interests or personal relationships that could have appeared to influence the work reported in this paper.

☐ The authors declare the following financial interests/personal relationships which may be considered as potential competing interests:

Journal Pre-proof